A neutron scattering study of the structure of a bimodal colloidal crystal

P. Bartlett[a] and R. H. Ottewill
School of Chemistry, Cantock's Close, University of Bristol, Bristol BS8 1TS, United Kingdom

(Received 11 September 1991; accepted 6 November 1991)

We have studied the freezing of a binary mixture of colloidal poly(methyl methacrylate) spheres of size ratio 0.31 and composition AB_4 (here A refers to the larger spheres). When suspended in a suitable liquid these particles interact via a steeply repulsive (approximately hard sphere) potential. The structure of the colloidal crystals formed in this binary system has been established from a combination of small-angle neutron and light scattering measurements. We find that there is an almost complete size separation on freezing. The crystalline phase contains almost exclusively large spheres while the smaller spheres are excluded from the crystal into a coexisting binary fluid. This observation is in agreement with recent density functional calculations for the freezing of hard sphere mixtures.

I. INTRODUCTION

One of the most distinctive features of colloidal systems is their ability to form a very diverse range of ordered structures with characteristic length scales which are much larger than atomic dimensions. This ordering is typically on a mesoscopic scale of 10–1000 nm. A well known example is the crystallization, at high densities, of strongly repulsive monodisperse spherical colloids.[1] The long range order is readily apparent from the iridescent colors seen in white light which arise from Bragg reflections from the ordered arrays of spherical particles.[2] Such colloidal systems can be considered as a supermolecular fluid of particles in a continuous background.[3] With this approach, thermodynamic properties (phase behavior, structure, etc.) can be understood in terms of standard statistical mechanical results developed for simple atomic liquids. Because all distances are thereby scaled up, the crystal structures are most conveniently studied by either light or small angle scattering techniques or imaged directly by microscopy.

In recent years colloidal particles with a narrow distribution of sizes have been synthesized[4] which interact only at closest approach through a steeply repulsive potential. When suspended in a liquid such systems,[5] with an appropriate change of scale, closely resemble the classical models of hard spheres widely studied in liquid state physics. This is evidenced by the phase behavior,[5,6] the equilibrium crystal structure,[7] and the osmotic compressibilities.[8] In particular, suspensions show a first-order phase transition from colloidal liquid to crystalline states with increasing volume fraction. The melting (φ_m) and freezing (φ_f) volume fractions are[6] within a few percent of those values found from Monte Carlo simulations of hard spheres.[9] Such colloidal systems offer the possibility of experimentally studying crystallization in an assembly of hard spheres, probably one of the simplest statistical systems to display a first-order fluid/solid phase transition. Here we use a suspension of colloidal "hard spheres" to follow the freezing transition in a binary mixture of hard spheres.

It has recently become possible to predict theoretically the phase diagram of simple systems by viewing the solid as a highly inhomogeneous liquid.[10] Density functional arguments are used to approximate the properties of this dense liquid. Generally these approximate theories are quite successful in describing the freezing of systems with short range repulsive interactions (although the results for softer, long range potentials are less reliable[10]). For example, the generalized effective liquid approximation of Lutsko and Baus[11] predicts almost quantitative agreement with the simulation data of Hoover and Ree[9] for a system of identically sized hard spheres, namely, a freezing volume fraction of $\varphi_f = 0.495$ and a melting value of $\varphi_m = 0.545$. Binary mixtures, however, present a much more demanding test of a freezing theory than does a one component system. In particular a fluid mixture may freeze into a much greater range of crystal structures than a single component fluid. The most efficient packing of two different sized hard spheres is not known, but will most probably depend critically on the ratio of the diameters $\alpha = d_B/d_A$, as well as the respective mole fractions. The simplest situation occurs when the hard sphere components are comparable in diameter. Here the stable solid phase is most likely a substitutionally disordered fcc or hcp crystal. With this assumption, both Zeng and Oxtoby[12] and Denton and Ashcroft[13] have described density functional theories for freezing in mixtures which are in very good agreement with the computer simulation results recently reported by Kranendonk and Frenkel[14] for diameter ratios in the range $0.85 \leqslant \alpha \leqslant 1.00$. However, for mixtures of hard spheres with a greater size disparity, $\alpha < 0.85$ say, there are significant disagreements between different density functional theories.[13,15–17] These theories differ only in the point at which the free energy perturbation expansion is truncated.

The freezing of a hard sphere mixture of arbitrary diameter ratio containing an equal concentration of small and large spheres was first considered by Smithline and Haymet[15] and Rick and Haymet.[16] These early calculations found that the disordered fcc structure, in which both small and large spheres are placed almost randomly on a common

[a] Author to whom correspondence should be addressed.

 0021-9606/92/043306-13$06.00

lattice, was stable at all size ratios. Different predictions come from the theory of Brami *et al.*[17] according to which the CsCl structure was stable for diameters $0.70 \leqslant \alpha \leqslant 0.75$ while the NaCl structure was stabilized at all ratios $\alpha \leqslant 0.46$. In the intervening gaps none of the solid phases investigated were found to be stable with respect to a binary fluid. Finally, the weighted density theory of Denton and Ashcroft,[13] which is in excellent agreement with simulation results for both a one and two component ($\alpha \geqslant 0.85$) system of hard spheres, predicts that for $\alpha < 0.76$ the two components are completely immiscible in a disordered fcc solid. The stable structure was found to be a pure fcc solid composed entirely of large spheres.

In an earlier study[18] we investigated the freezing of a binary mixture of colloidal hard spheres of diameter ratio $\alpha = 0.61$. The particles were sterically stabilized poly(methyl methacrylate) spheres. If it is assumed that the fluid in which the colloidal particles were suspended plays no structural role then these experiments may be directly compared with results for hard sphere mixtures. This amounts to an assumption that the one-body "embedding" energies are constant, independent of the positions of the colloidal species. Suspensions containing approximately equal number densities of large and small spheres, froze into a close packed crystal composed almost entirely of large spheres (in agreement with the predictions of Denton and Ashcroft[13]). However, experiments demonstrated that the structure of the stable solid phase was a strong function of the composition. Suspensions, richer in small spheres than large spheres, froze into either an AB_2 or an AB_{13} structure.[19] In the present investigation we again consider a binary mixture of large and small colloidal spheres, but now one where the second component is sufficiently small ($\alpha = 0.31$) so that it could be introduced into the interstitial sites in a crystal of large spheres. In this limit a fluid mixture may freeze, in principle, into any one of a very diverse class of crystal structures based on either full or partial occupancy of the vacant octahedral and tetrahedral sites in an assembly of large spheres. The octahedral sites are the most obvious choice for the largest possible small sphere with a maximum diameter ratio of 0.414 in a close-packed fcc lattice. Complete filling of the octahedral vacancies gives a structure equivalent to that found in NaCl. The question which motivated this study is whether, in a mixture of colloidal hard spheres of diameter ratio $\alpha = 0.31$, freezing occurs into such an interstitial structure or is there, as predicted by Denton and Ashcroft,[13] a solid state phase separation. To answer this question we have studied the structure of the solid phase formed at high densities by a mixture of hard sphere colloids with small-angle neutron and light scattering measurements combined with direct observation by electron microscopy. In particular, by studying the small-angle neutron scattering (SANS) from a mixture of hydrogenated and deuterated colloidal spheres at different medium contrasts we have unambiguously separated the small-sphere structure from that of the larger spheres.

The remainder of this paper is as follows. Sample preparation, and the experimental aspects of the small-angle neutron and light scattering measurements are discussed in Sec. II. In Sec. III we describe the theory of scattering from both dilute and concentrated bimodal mixtures of colloidal poly (methyl methacrylate) spheres. We treat each different sized colloidal species in terms of a polydisperse core–shell model. Finally, we present our results in Sec. IV and summarize our conclusions in Sec. V.

II. EXPERIMENTAL DETAILS

A. Sample description and characterization

Three different sets of colloidal poly(methyl methacrylate) spheres were used in the present study. All the particles had a common core–shell structure. The core, of either hydrogenated or deuterated poly(methyl methacrylate) (PMMA), was surrounded by an outer hydrogenated stabilizing layer of a grafted comb copolymer with poly(12-hydroxystearic acid) (PHS) "teeth" and a poly(glycidyl methacrylate/methyl methacrylate) backbone. The largest spheres (component A), here labeled *h*-PBM1, were fully hydrogenated while the two sets of approximately equal-sized smaller spheres (component B) consisted of either hydrogenated (*h*-PBM11) or deuterated cores (*d*-PBM14) and hydrogenated stabilizers. The hydrogenated particles were synthesised by methods similar to those described previously.[4] While the deuterated sample (*d*-PBM14) was prepared by repeating the synthesis of the hydrogenated latex, *h*-PBM11, with the hydrogenated monomer replaced by fully deuterated methyl methacrylate.[20]

The number average diameter $\bar{d}$ and polydispersity σ_d (standard deviation of the diameter distribution divided by its mean) of each system was determined by electron microscopy. The results are listed in Table I. Comparable diameters were found from dynamic light scattering measurements. Table I also gives the results, for *h*-PBM1 and *d*-PBM14 only, of a least squares fit of the measured form factors in *cis* h_{18}-decalin to the polydisperse core–shell model, described in Sec. III A. These results will be described in greater detail

TABLE I. Characterization of the colloidal particles.

System	Diameter (nm) DLS $\bar{d}_h$	SANS $2(\bar{r}+\Delta)$	TEM $\bar{d}$	Polydispersity TEM σ_d	Specific Volume ($cm^3\,g^{-1}$)
h-PBM1	315 ± 2	311 ± 2	332 ± 17	0.05	0.853 ± 0.002
h-PBM11	110 ± 2	···	124 ± 12	0.09	0.854 ± 0.002
d-PBM14	97 ± 2	93 ± 1	120 ± 12	0.13	0.791[a]

[a] Estimated from the isotopic composition.

in Sec. IV. Combining these measurements the diameter ratio $\alpha = d_B/d_A$ is approximately 0.31 ± 0.01, for a binary system of *h*-PBM1 and *d*-PBM14 and 0.36 ± 0.01 for the *h*-PBM1/*h*-PBM11 combination.

Table I also quotes values for the specific volumes of the hydrogenated particles in decalin. The values refer to the suspension volume increase per unit mass of added (dried) colloidal material. The measured values differ slightly from that found for bulk PMMA ($\approx 0.842\ cm^3\ g^{-1}$) as a result of the excluded volume of the PHS chains. Because of the, as yet, incomplete characterization of the stabilizing layer, it is impossible to calculate reliably the suspension volume fraction from this data. Here an alternative approach was used to fix the suspension volume fraction. As in previous studies,[5] the interparticle potential was assumed to be "hard sphere" in character and the concentration at which crystallization first occurred was identified with the value found, from computer simulation,[9] for the freezing point in a system of hard spheres, namely $\varphi_f = 0.494$. All other concentrations were scaled by the same factor to provide effective hard sphere volume fractions (φ).

The phase behavior of the large hydrogenated spheres (*h*-PBM1) was followed in *cis*-decalin. Using the experimentally determined density (Table I), freezing and melting was observed at core volume fractions (φ_c) of 0.414 ± 0.005 and 0.448 ± 0.005, respectively. The difference between the experimentally determined core freezing density and the known hard sphere freezing volume fraction of 0.494 was attributed to the thickness of the stabilizing layer. Using a value for the mean core radius of 147 nm (see Sec. IV A) the shell thickness Δ was calculated as 8.9 ± 0.6 nm, in excellent agreement with the chain length expected[4] for a fully extended PHS molecule (~ 9 nm). The corresponding effective volume fraction at melting was 0.534 ± 0.006 in reasonable agreement with the simulation result,[9] for hard spheres, of $\varphi_m = 0.545$.

A different approach was necessary to determine the effective volume fraction for suspensions of the smaller spheres (*h*-PBM11 or *d*-PBM14). These suspensions remained amorphous at all concentrations with no sign of a fluid–solid phase transition. The reasons for the absence of a phase transition are not fully understood, but it seems likely that the significantly larger polydispersities ($\sigma_d \sim 0.13$) found for the small spheres, as opposed to $\sigma_d \sim 0.04$ for the larger spheres, is important. Theoretical[21,22] results suggest that the fluid–solid phase transition is suppressed for polydispersities in excess of some critical value σ^*. Estimates for σ^* vary but typically lie in the range 0.05–0.11. In the absence of freezing data, the effective volume fraction of the small spheres was determined by assuming the shell thickness Δ was unchanged from the value found for the larger spheres ($\Delta \sim 8.9$ nm). For the deuterated small sphere, where the core radius was 37.5 nm (see Sec. IV A) this gave the effective volume fraction (φ) as 1.90 ± 0.08 times the core volume fraction (φ_c).

Table II gives the effective component volume fractions and compositions of the suspensions studied. All bimodal samples showed rapid crystallization within a few hours. Visual observation showed that, at the time of both neutron and light scattering experiments, the samples contained a homogeneously nucleated powder of small (~ 10–$30\ \mu m$) randomly orientated Bragg reflecting crystallites.

B. SANS measurements

The neutron scattering experiments were carried out at the Institute Laue-Langevin, Grenoble on the diffractometer D11. The particles were dispersed in a mixture of *cis* h_{18}-decalin and d_{18}-octane. The coherent scattering length density of the suspension medium was varied by altering the relative proportions of the hydrogenated and deuterated hydrocarbons. The colloidal suspensions were contained in 1 mm pathlength quartz cells thermostatted at 25 °C. Measurements were made at a sample–detector distance of 35.7 m and a source to sample distance ("collimation length") of approximately 40 m. The effective source was the exit of a neutron guide 3 cm wide and 5 cm high.[23] Defining apertures were placed in front of the sample to collimate the incident neutron beam. At the sample position the beam was approximately rectangular with a vertical height of approximately 1.5 cm and a width of 1 cm. The incident wavelength distribution was triangular[23] and centered on the wavelength $\lambda = 1$ nm with a full width at half-maximum (FWHM) of 0.09 nm. This gave an experimentally accessible q range of 0.01 to 0.08 nm^{-1}. The scattering intensity data was collected on a two-dimensional detector and averaged radially. Corrections for sample attenuation and scattering from the quartz cell were made by standard ILL pro-

TABLE II. Component volume fractions and number densities of the suspensions studied. Here A labels the larger and B the smaller species.

Sample	Component A	Component B	Suspension medium	φ_A	φ_B	n_B/n_A
1	*h*-PBM1	*d*-PBM14	*cis* h_{18}-decalin d_{18}-octane	0.540 ± 0.007	0.067 ± 0.003	4.2 ± 0.4
2	*h*-PBM1	*h*-PBM11	*cis* h_{18}-decalin CS_2	0.538 ± 0.007	0	0
3	"	"	"	0.538 ± 0.007	0.035 ± 0.002	1.4 ± 0.1
4	"	"	"	0.545 ± 0.007	0.051 ± 0.002	2.0 ± 0.2
5	"	"	"	0.534 ± 0.007	0.070 ± 0.003	2.8 ± 0.3

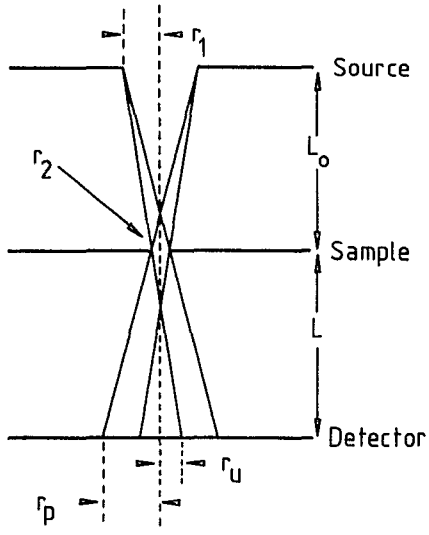

FIG. 1. A schematic illustration of the scattering geometry used in the SANS experiments. The plane of the paper corresponds to the scattering plane. For the calculation of the smearing corrections the source and sample apertures are assumed circular of radii r_1 and r_2, respectively. The distance between apertures is L_0 and the distance from the sample to the plane of the detector is L. At the detector the beam intensity is trapezoidal in section with collimation shadows at distances r_u and r_p.

cedures. At 35.7 m the incoherent scattering was of very low intensity and was neglected. Using the measured scattering from water, at a sample–detector distance of 5 m, the data was further corrected for detector sensitivity and converted into absolute units.

The experimentally measured scattering data is expected to differ from theoretical curves as a result of two instrumental factors: first, the limited resolution of the diffractometer and second, the influence of multiple scattering. Here it is assumed that these two corrections can be treated independently of each other.

With an instrument set to detect radiation with a mean scattering vector $\bar{\mathbf{q}}$ (here the bar denotes the average value of a parameter), radiation with scattering vector $\mathbf{q}$ in a range around $\bar{\mathbf{q}}$ also contributes as a result of the finite divergence of the incident beam, the spread in neutron wavelengths, and the positional resolution of the 2D detector. Here for simplicity, we ignore the rectangular shape of the incident beam. Instead it was assumed that resolution effects could be described in terms of, a suitably averaged, circular geometry. Figure 1 shows a schematic representation of an approximately equivalent aperture geometry. The source and defining apertures are circular with radii r_1 and r_2, respectively, and are uniformly illuminated. For such a geometry, the image of the source on the detector is trapezoidal in shape with the radius, at the detector, of the beam umbra and penumbra shadows as

$$r_u = \frac{L}{L_0} r_1 - \left(1 + \frac{L}{L_0}\right) r_2,$$
$$r_p = \frac{L}{L_0} r_1 + \left(1 + \frac{L}{L_0}\right) r_2, \tag{1}$$

respectively. Here L_0 is the source–sample and L the sample–detector distance. For the present geometry, the sizes of the apertures were fixed at $r_1 = 2$ cm and $r_2 = 0.5$ cm, intermediate between the horizontal and vertical dimensions of the actual instrument apertures. Calculations showed that the resolution corrections were little changed if a slightly different choice of aperture sizes was used.

The importance of making such resolution corrections is shown by a simple calculation. The full width at half-maximum (FWHM) Δq of the resolution function is approximately

$$\frac{\Delta q}{\bar{q}} = \left[\left(\frac{\Delta\lambda}{\bar{\lambda}}\right)^2 + \frac{\Delta\vartheta^2}{4\tan^2\bar{\vartheta}/2}\right]^{1/2}, \tag{2}$$

where $\Delta\lambda$ and $\Delta\vartheta$ are the corresponding (FWHM) widths of the wavelength and intensity distributions respectively. $\Delta\vartheta$ is the angle where the intensity of the source image on the detector is reduced to half its maximum value, which is given as $\Delta\vartheta = 2r_1/L$. Equation (2) predicts that for the current geometry, $\Delta q/\bar{q}$ varies between ~ 0.6 for the smallest scattering vector to ~ 0.1 for the largest scattering vectors. Hence resolution corrections can be expected to have a significant effect on the scattering data, particularly at low q.

The accurate treatment of instrumental smearing in circularly symmetric small-angle scattering experiments has been described in detail by several authors.[24–26] Here we follow the approach suggested by Ramakrishnan.[25] The observed intensity $\Delta\mathbf{I}^{\text{obs}}$, scattered within the solid angle $\Delta\omega$, at an apparent scattering vector $\bar{\mathbf{q}}$ from a primary beam of intensity $\mathbf{I}_0$ is given by the expression

$$\frac{\Delta I^{\text{obs}}}{\Delta\omega}(\bar{\mathbf{q}}) = \mathbf{I}_0 TD \int \mathbf{I}_1\left(\frac{\bar{\lambda}}{\lambda}\bar{\mathbf{q}}\right) S(\lambda)\, d\lambda, \tag{3}$$

where $S(\lambda)$ is the normalized wavelength distribution, T is the sample transmission, and D is the sample thickness. The effective differential scattering cross section per unit volume $\mathbf{I}_1(\mathbf{q})$ is a two-dimensional convolution of the theoretical cross section $d\Sigma/d\omega$ with $W(\mathbf{q})$, the intensity distribution of the incident beam on the detector, and $R(\mathbf{q})$ the detector resolution function. For isotropic scatterers with symmetric illumination the functions $d\Sigma/d\omega$, W, and R depend only on the magnitude of the scattering vector $q = |\mathbf{q}|$ and the analysis is considerably simplified. In such a case, the smeared intensity $\mathbf{I}_1(q)$ is given by the one-dimensional integral

$$\mathbf{I}_1(q) = \int_0^\infty \left\{\widetilde{\frac{d\Sigma}{d\omega}}(r)\cdot\tilde{W}(r)\cdot\tilde{R}(r)\right\} r J_0(qr)\, dr, \tag{4}$$

where $\tilde{f}(\tilde{r})$ denotes the Hankel transform of the function $f(q)$, which is given by the expression

$$\tilde{f}(r) = \int_0^\infty f(q) q J_0(qr)\, dq. \tag{5}$$

Resolution corrections were made using the triangular wavelength distribution $S(\lambda)$ described by Ibel,[23] a trapezoidal beam profile,[24] and a Gaussian detector resolution function $R(q)$ with a FWHM equal to the detector cell size of 1 cm.

Multiple scattering effects will also distort the observed scattering patterns. For example, in dilute samples multiple scattering fills in the minima in the particle form factors and

increases the measured differential cross section above the theoretical (Born) value. Although the general treatment of multiple scattering is a delicate problem, analytic expressions for the distortion of the scattering have been derived by Schelten and Schmatz[27] under the assumption, fulfilled here, that scattering occurs only at small angles. In their analysis multiple scattering is analyzed in terms of Hankel transforms of the relevant functions. The transform of the measured cross section $(d\Sigma/d\omega)_{ms}$, determined from a experiment in which multiple scattering occurs, is given by the expression

$$\left(\frac{\widetilde{d\Sigma}}{d\omega}\right)_{ms}(r) = \frac{\bar{k}^2}{D}\exp(\tilde{s}(r)/\bar{k}^2). \tag{6}$$

Here $\bar{k}$ is the mean wave number of the incident neutron beam $(2\pi/\bar{\lambda})$, and $\tilde{s}(r)$ is the transform of the theoretical scattering probability $s(q) = D\,d\Sigma/d\omega$.

In cases where both multiple scattering and smearing corrections are significant then, to a first approximation, the intensity is given by Eqs. (3) and (4) with the transform of the theoretical scattering cross section replaced by the multiple scattering result [Eq. (6)]. In the current experiments, with sample path lengths of 1 mm, slight multiple scattering occured in strongly scattering samples. We have, nevertheless, used this path length so as to ensure sufficient scattering into the detector at all medium contrasts. The multiple scattering corrections required, as calculated from Eq. (6), were fairly minor. Their inclusion was however found necessary to achieve a detailed agreement between theory and experiment.

C. Light scattering measurements

The limited resolution of small-angle neutron scattering experiments becomes very apparent when highly correlated structures with large repeat distances, such as colloidal crystals, are studied. In such cases light scattering measurements are particularly valuable because the typical resolution $(\Delta q/q)$ of light scattering experiments may be an order of magnitude smaller, for the same scattering vector $\mathbf{q}$, as a SANS measurements. Note, however, that SANS provides a much wider range of scattering vectors.

As a result of the significant refractive index mismatch between the PMMA particles ($n\sim1.49$) and *cis*-decalin ($n\sim1.48$) the pure hydrocarbon suspensions used show strong multiple scattering of light. Hence light and neutron scattering measurements could not be made on the same experimental sample. Almost index matched samples were prepared using a mixed suspension medium of carbon disulphide (mass fraction ~0.25) and *cis*-decalin. Previous studies have shown that changing the suspension medium in this way has no significant effect on the suspension microstructure.

Light scattering measurements were made on mixtures of *h*-PBM1 and *h*-PBM11. The scattered intensity was measured at scattering angles between $\vartheta = 20°$ and 140°, in angular steps of 0.25°, using an automated light scattering diffractometer described elsewhere.[7] This gave a range of scattering vectors between 0.005 and 0.04 nm^{-1}; overlapping with the q range of the SANS measurements. The instrument had an angular resolution (FWHM) of approximately 0.5°. The fractional q resolution $(\Delta q/q)$ improved from ~0.02 at $q\sim0.005$ nm^{-1} to a figure in excess of 0.002 at $q\sim0.04$ nm^{-1}.

III. SCATTERING THEORY

A. The form factor of polydisperse core–shell spheres

The theory of small-angle neutron scattering from a suspension of colloidal particles has been described by, e.g., Hayter.[28] In the absence of multiple or incoherent scattering, the measured intensity is proportional to the coherent portion of the differential cross section per unit volume

$$\frac{d\Sigma}{d\omega}(\mathbf{q}) = \frac{1}{V}\left\langle \sum_{ij} b_i b_j^* \exp[i\mathbf{q}\cdot(\mathbf{r}_i - \mathbf{r}_j)] \right\rangle, \tag{7}$$

where b_i is the (bound) coherent scattering length of the chemical species at the position $\mathbf{r}_i$, V is the sample volume and the brackets describe a thermal average over all possible equilibrium configurations. The scattering vector $\mathbf{q}$ is the difference between the wave vectors of the incident and scattered radiation with the magnitude $|\mathbf{q}| = (4\pi/\lambda)\sin(\vartheta/2)$, where ϑ is the scattering angle at which the neutron radiation of wavelength λ is observed. For a suspension of monodisperse noninteracting particles, there is no phase coherence between waves scattered from different particles so that Eq. (7) becomes

$$\frac{d\Sigma}{d\omega}(\mathbf{q}) = n\left\langle \left| \sum_{i(v)} b_i \exp(i\mathbf{q}\cdot\mathbf{r}_i) \right|^2 \right\rangle, \tag{8}$$

where n is the number density of particles, and the sum is over all atoms in the particle volume v. At the small scattering vectors typically explored in a SANS experiment, the intensity is insensitive to details on the atomic scale so that we can replace the atomic scattering lengths b_i by the locally averaged scattering length density defined as

$$\rho(\mathbf{r}) = \sum_i b_i \delta(\mathbf{r} - \mathbf{r}_i), \tag{9}$$

where b_i is the scattering length of the atom at the position $\mathbf{r}_i$. Replacing the sum in Eq. (8) by an integration yields an expression for the scattering from a suspension of noninteracting spheres

$$\frac{d\Sigma}{d\omega}(\mathbf{q}) = nF(\mathbf{q})^2, \tag{10}$$

where the single particle amplitude is defined by the Fourier transform

$$F(\mathbf{q}) = \int [\rho(\mathbf{r}) - \rho_m]\exp(i\mathbf{q}\cdot\mathbf{r})d\mathbf{r}. \tag{11}$$

Here ρ_m is the scattering length density of the suspension medium. In the case of a spherically symmetric profile $\rho(r)$, the expression for the single particle amplitude reduces to

$$F(q) = 4\pi\int r^2[\rho(r) - \rho_m]\frac{\sin qr}{qr}dr. \tag{12}$$

In previous work[20] it has been shown that the PHS-PMMA spheres used in the present study may be, at least approximately, described by a two-shell model, e.g., an inner-PMMA core and an outer shell of solvated PHS stabilizing

chains. For such a model, the scattering profile has the approximate form

$$\rho(r) = \begin{cases} \rho_c & r \leq r_c \\ \rho_s & r_c < r \leq r_c + \Delta \end{cases}, \tag{13}$$

where the spherical core of radius r_c and scattering length density ρ_c is surrounded by a shell of thickness Δ and scattering length density ρ_s. The corresponding particle scattering amplitude follows from Eq. (12) as

$$F(x) = \frac{4\pi}{q^3}(\rho_s - \rho_c)\{\gamma j(x + \delta x) - j(x)\}, \tag{14}$$

where x is the dimensionless variable qr_c, $\delta = \Delta/r_c$, and the function $j(x) = \sin x - x \cos x$. γ is the scaled medium contrast, $\gamma = (\rho_m - \rho_s)/(\rho_c - \rho_s)$, and determines the relative proportion of the scattering from the core or shell. For $\gamma = 0$ only the core scatters ($\rho_m = \rho_s$), while for $\gamma = 1$ the shell alone contributes to the total intensity ($\rho_m = \rho_c$). At the matchpoint, where the scattered intensity at $q = 0$ vanishes, $\gamma = (1 + \delta)^{-3}$.

Colloidal particles are never identical in size. There is always a distribution of particle diameters. To treat this size polydispersity, Eq. (10) must be averaged over the particle size distribution. Here we assume that there is a distribution only of the particle core sizes while the shell thickness Δ is fixed for all spheres by the molecular geometry of the grafted PHS chains. In this case the single particle form factor $F^2(qr_c)$ is replaced by the size average

$$\overline{F^2}(q\bar{r}_c) = \int_0^\infty G(r_c) F^2(qr_c)\, dr_c, \tag{15}$$

where $G(r_c)$ is the normalized probability of finding a particle with a core radius between r_c and $r_c + dr_c$, and $\bar{r}_c$ is the mean core radius. Equation (15) has been evaluated numerically for a wide range of distribution functions.[29] Here we choose the Schulz distribution,[30] which is both physically realistic as well as mathematically tractable. The normalized form of this distribution is

$$G(r_c) = \frac{r_c^Z}{\Gamma(Z+1)}\left(\frac{Z+1}{\bar{r}_c}\right)^{Z+1} \times \exp\left[-\frac{r_c}{\bar{r}_c}(Z+1)\right], \tag{16}$$

where $\bar{r}_c$ is the mean core radius and Z is related to the normalized second moment (or polydispersity) σ_c of the particle core radius distribution by the expression

$$\sigma_c^2 = \left(\frac{\overline{r_c^2}}{\bar{r}_c^2} - 1\right) = \frac{1}{Z+1}. \tag{17}$$

For finite Z the Schulz distribution has the realistic feature that it is skewed towards large sizes. With increasing Z, Eq. (16) asymptotically approaches a Gaussian and, in the limit of $Z \to \infty$, tends to a delta function at $\bar{r}_c$.

The size-averaged scattering function for a Schulz distributed system of core–shell spheres follows from Eqs. (14), (15), and (16) as

$$\begin{aligned}\overline{F^2}(\bar{x}) = \frac{16\pi^2}{q^6}(\rho_s - \rho_c)^2 \Big\{ & c_1 + c_2\bar{x} + c_3\bar{x}^2\left(\frac{Z+2}{Z+1}\right) \\ & + B(\bar{x})^{(z+1)/2}(c_4 \cos[(Z+1)D(\bar{x})] + c_7 \sin[(Z+1)D(\bar{x})]) \\ & + \bar{x}B(\bar{x})^{(z+2)/2}(c_5 \cos[(Z+2)D(\bar{x})] + c_8 \sin[(Z+2)D(\bar{x})]) \\ & + \left(\frac{Z+2}{Z+1}\right)\bar{x}^2 B(\bar{x})^{(z+3)/2}(c_6 \cos[(Z+3)D(\bar{x})] + c_9 \sin[(Z+3)D(\bar{x})])\Big\},\end{aligned} \tag{18}$$

where the functions $B(\bar{x})$ and $D(\bar{x})$ are defined as

$$B(\bar{x}) = \frac{(Z+1)^2}{(Z+1)^2 + 4\bar{x}^2}, \quad D(\bar{x}) = \tan^{-1}\left(\frac{2\bar{x}}{Z+1}\right), \tag{19}$$

with $\bar{x} = q\bar{r}_c$ and the coefficients c_i are given by the expressions

$$\begin{aligned} c_1 &= \tfrac{1}{2} - \gamma(\cos y + y \sin y) + \frac{\gamma^2}{2}(1 + y^2), \\ c_2 &= \gamma y(\gamma - \cos y), \\ c_3 &= \frac{\gamma^2 + 1}{2} - \gamma \cos y, \\ c_4 &= \gamma^2(y \cos y - \sin y)^2 - c_1, \\ c_5 &= 2\gamma \sin y[1 - \gamma(y \sin y + \cos y)] + c_2, \\ c_6 &= c_3 - \gamma^2 \sin^2 y, \\ c_7 &= \gamma \sin y - \frac{\gamma^2}{2}(1 + y^2)\sin 2y - c_5, \\ c_8 &= c_4 - \tfrac{1}{2} + \gamma \cos y - \frac{\gamma^2}{2}(1 + y^2)\cos 2y \\ c_9 &= \gamma \sin y(1 - \gamma \cos y). \end{aligned} \tag{20}$$

with $y = q\Delta$. For $\gamma = 0$, where the shell is effectively transparent, this result reduces to that given by Aragon and Pecora[31] for the scattering from a Schulz distribution of homogeneous spheres.

B. The scattering from a concentrated multicomponent suspension

In a concentrated suspension the positions of the centers of each particle are correlated so that interparticle interference effects appear in the scattered intensity. The general expression for the scattering from a multicomponent system

of such interacting particles has been given by Guinier and Fournet.[32] Here, for completeness, we repeat the principal equations before considering, in Sec. III C, the specific case of a bimodal suspension. Labeling the different sized colloidal species as $\alpha, \beta \cdots$, and the component particles of each species by $N, M \cdots$, etc., the position vector $\mathbf{r}_i$ of the ith nucleus may be written as $\mathbf{r}_{iN}^{\alpha} + \mathbf{R}_N^{\alpha}$, where $\mathbf{R}_N^{\alpha}$ is the center of mass of the N th particle of species α and $\mathbf{r}_{iN}^{\alpha}$ is the position vector of the ith nucleus relative to this point. With this substitution the scattered intensity from a system of ν different sized colloidal species may be separated into terms describing separately the intraparticle and interparticle correlations

$$\frac{d\Sigma}{d\omega}(\mathbf{q}) = \sum_{\alpha=1}^{\nu}\sum_{\beta=1}^{\nu}(n_\alpha n_\beta)^{1/2}F_\alpha(\mathbf{q})F_\beta^*(\mathbf{q})S_{\alpha\beta}(\mathbf{q}). \tag{21}$$

Here $F_\alpha(\mathbf{q})$ is the single particle scattering amplitude of species α defined following Eq. (12), n_α is the number density of species α and $S_{\alpha\beta}(\mathbf{q})$ is the structure factor which describes the correlations between the centers of species α and β. $S_{\alpha\beta}$ is essentially the Fourier transform of the radial distribution function $g_{\alpha\beta}(\mathbf{R})$, which measures the probability of finding a particle of species β at a vector distance $\mathbf{R}$ from a reference particle of species α. Following Kirkwood and Buff[33] $S_{\alpha\beta}$ is defined by the ensemble average

$$S_{\alpha\beta}(\mathbf{q}) = \frac{1}{[\langle N_\alpha\rangle\langle N_\beta\rangle]^{1/2}} \times\left\langle\sum_{N=1}^{N_\alpha}\sum_{M=1}^{N_\beta}\exp[i\mathbf{q}\cdot(\mathbf{R}_N^{\alpha}-\mathbf{R}_M^{\beta})]\right\rangle, \tag{22}$$

which may be rewritten in terms of the partial radial distribution function $g_{\alpha\beta}$ as

$$S_{\alpha\beta}(\mathbf{q}) = \delta_{\alpha\beta} + (n_\alpha n_\beta)^{1/2}\int\exp(i\mathbf{q}\cdot\mathbf{R})[g_{\alpha\beta}(\mathbf{R})-1]d\mathbf{R} + (2\pi)^3(n_\alpha n_\beta)^{1/2}\delta(\mathbf{q}). \tag{23}$$

We shall ignore the delta function in Eq. (23) which corresponds to pure forward scattering from the suspension. In the particular case where all interactions are spherically symmetric $S_{\alpha\beta}(\mathbf{q})$ is a function only of $q = |\mathbf{q}|$ and Eq. (23) simplifies to

$$S_{\alpha\beta}(q) = \delta_{\alpha\beta} + 4\pi(n_\alpha n_\beta)^{1/2}\int R^2[g_{\alpha\beta}(R)-1]\times\frac{\sin qR}{qR}dR. \tag{24}$$

For an isotropic binary suspension (i.e., $\nu = 2$), Eq. (21) reduces to the expression

$$\frac{d\Sigma}{d\omega}(q) = n_\alpha F_\alpha^2(q)S_{\alpha\alpha}(q) + 2(n_\alpha n_\beta)^{1/2}F_\alpha(q)\times F_\beta(q)S_{\alpha\beta}(q) + n_\beta F_\beta^2(q)S_{\beta\beta}(q). \tag{25}$$

C. Bimodal suspensions

A bimodal suspension consists of a mixture of two sets of very differently sized colloidal spheres, here distinguished as A and B. Provided the difference in the mean sizes is greater than the combined width of each diameter distribution, then the scattering from such a bimodal suspension can, to a first approximation, be treated in terms of a purely binary mixture of spheres. For an exact calculation of the scattering from a bimodal suspension we proceed by rewritting Eq. (21) in a form analogous to Eq. (25)

$$\frac{d\Sigma}{d\omega}(q) = n_{\mathrm{A}}\,\overline{F_{\mathrm{A}}^2}(q)\bar{S}_{\mathrm{AA}}(q) + 2(n_{\mathrm{A}}n_{\mathrm{B}})^{1/2}\left[\,\overline{F_{\mathrm{A}}^2}(q)\,\overline{F_{\mathrm{B}}^2}(q)\,\right]^{1/2}\bar{S}_{\mathrm{AB}}(q) + n_{\mathrm{B}}\,\overline{F_{\mathrm{B}}^2}(q)\bar{S}_{\mathrm{BB}}(q), \tag{26}$$

where the subscripts identify the parent colloidal system, A or B, and the system number densities, polydisperse form factors and partial structure factors are given by the expressions

$$\begin{aligned}
n_{\mathrm{A}} &= \sum_{\alpha_{\mathrm{A}}=1}^{\nu_{\mathrm{A}}} n_{\alpha_{\mathrm{A}}}, \quad n_{\mathrm{B}} = \sum_{\alpha_{\mathrm{B}}=1}^{\nu_{\mathrm{B}}} n_{\alpha_{\mathrm{B}}},\\
\overline{F_{\mathrm{A}}^2} &= \sum_{\alpha_{\mathrm{A}}=1}^{\nu_{\mathrm{A}}} n_{\alpha_{\mathrm{A}}}F_{\alpha_{\mathrm{A}}}^2 \Big/ \sum_{\alpha_{\mathrm{A}}=1}^{\nu_{\mathrm{A}}} n_{\alpha_{\mathrm{A}}},\\
\overline{F_{\mathrm{B}}^2} &= \sum_{\alpha_{\mathrm{B}}=1}^{\nu_{\mathrm{B}}} n_{\alpha_{\mathrm{B}}}F_{\alpha_{\mathrm{B}}}^2 \Big/ \sum_{\alpha_{\mathrm{B}}=1}^{\nu_{\mathrm{B}}} n_{\alpha_{\mathrm{B}}},\\
\bar{S}_{\mathrm{AA}} &= \sum_{\alpha_{\mathrm{A}},\beta_{\mathrm{A}}=1}^{\nu_{\mathrm{A}}} (n_{\alpha_{\mathrm{A}}}n_{\beta_{\mathrm{A}}})^{1/2}F_{\alpha_{\mathrm{A}}}F_{\beta_{\mathrm{A}}}S_{\alpha_{\mathrm{A}}\beta_{\mathrm{A}}} \Big/ \sum_{\alpha_{\mathrm{A}}=1}^{\nu_{\mathrm{A}}} n_{\alpha_{\mathrm{A}}}F_{\alpha_{\mathrm{A}}}^2,\\
\bar{S}_{\mathrm{AB}} &= \sum_{\alpha_{\mathrm{A}}=1}^{\nu_{\mathrm{A}}}\sum_{\beta_{\mathrm{B}}=1}^{\nu_{\mathrm{B}}} (n_{\alpha_{\mathrm{A}}}n_{\beta_{\mathrm{B}}})^{1/2}F_{\alpha_{\mathrm{A}}}F_{\beta_{\mathrm{B}}}S_{\alpha_{\mathrm{A}}\beta_{\mathrm{B}}} \Big/ \left[\sum_{\alpha_{\mathrm{A}}=1}^{\nu_{\mathrm{A}}} n_{\alpha_{\mathrm{A}}}F_{\alpha_{\mathrm{A}}}^2 \sum_{\alpha_{\mathrm{B}}=1}^{\nu_{\mathrm{B}}} n_{\alpha_{\mathrm{B}}}F_{\alpha_{\mathrm{B}}}^2\right]^{1/2},\\
\bar{S}_{\mathrm{BB}} &= \sum_{\alpha_{\mathrm{B}},\beta_{\mathrm{B}}=1}^{\nu_{\mathrm{B}}} (n_{\alpha_{\mathrm{B}}}n_{\beta_{\mathrm{B}}})^{1/2}F_{\alpha_{\mathrm{B}}}F_{\beta_{\mathrm{B}}}S_{\alpha_{\mathrm{B}}\beta_{\mathrm{B}}} \Big/ \sum_{\alpha_{\mathrm{B}}=1}^{\nu_{\mathrm{B}}} n_{\alpha_{\mathrm{B}}}F_{\alpha_{\mathrm{B}}}^2.
\end{aligned} \tag{27}$$

Here ν_{A} and ν_{B} are the number of particle species comprising each colloidal system (so that $\nu_{\mathrm{A}} + \nu_{\mathrm{B}} = \nu$) and the positive value of the square root is to be taken.

To treat a completely polydisperse suspension the summations in Eq. (27) should be replaced by integrations over the component particle size distributions. In the case of vanishing size polydispersity (i.e., $\sigma_{\mathrm{A}}, \sigma_{\mathrm{B}} \to 0$) it is apparent from Eq. (27) that the polydisperse self-structure factors $\bar{S}_{\mathrm{AA}}(q)$ and $\bar{S}_{\mathrm{BB}}(q)$ approach asymptotically the correct binary limiting functions $S_{\alpha\alpha}(q)$ and $S_{\beta\beta}(q)$, where α and β are the species of mean diameters $\bar{d}_{\mathrm{A}}$ and $\bar{d}_{\mathrm{B}}$. However, by contrast the polydisperse cross structure factor $\bar{S}_{\mathrm{AB}}(q)$ reduces, in this limit, to $\pm S_{\alpha\beta}(q)$ rather than the expected limiting form $S_{\alpha\beta}(q)$. The sign is determined by the relative phases of the scattering amplitudes from particles of type α and β [i.e., the sign of the product $F_\alpha(q)F_\beta(q)$]. For a spherically symmetric scattering profile $\rho(r)$ the scattered amplitude $F(q)$ changes sign at the position of the minima $q_{\min}$ in the form factor $F(q)$. Hence in the limit $\sigma_{\mathrm{A}}, \sigma_{\mathrm{B}} \to 0$, the polydisperse cross structure factor $\bar{S}_{\mathrm{AB}}(q)$ shows a singularity at $q_{\min}$. Although other polydisperse structure factor definitions are possible which ensure that $\bar{S}_{\mathrm{AB}}(q)$ approaches $S_{\alpha\beta}(q)$ at all q. The present choice has the advantage that information can be obtained directly from

experiment without the need for additional assumptions about the the relative phase of the individual form factors.

Note that the polydisperse structure factors, defined in Eq. (27), are not independent of the scattering amplitudes $F(q)$ as is the case for a pure binary mixture. However, as will become apparent later, the dependence of the derived structure factors on ρ_m is negligible in most cases and may normally be ignored.

Finally, the differential scattering cross section given in Eq. (26) is an experimentally observable quantity, and hence must always be positive for all values of $n_A \overline{F_A^2}(q)$ and $n_B \overline{F_B^2}(q)$. From the theory of quadratic forms it follows that the polydisperse structure factors must satisfy the conditions

$$\bar{S}_{AA}(q) \geq 0, \quad \bar{S}_{BB}(q) \geq 0,$$
$$\bar{S}_{AA}(q)\bar{S}_{BB}(q) - \bar{S}_{AB}^2(q) \geq 0 \tag{28}$$

at each value of q.

IV. RESULTS AND DISCUSSION

A. Dilute samples

An understanding of the dependence of the polydisperse form factors $\overline{F_A^2}(q)$ and $\overline{F_B^2}(q)$ upon the medium contrast ρ_m is an essential first step to evaluating the partial structure factors $\overline{S_{ij}}(q)$. For a single component suspension with a sufficiently low number density so that interparticle interactions are negligible, the scattered intensity is simply proportional to the form factor $\overline{F^2}(q)$. Knowledge of the number density n gives the polydisperse form factor directly.

SANS measurements were made on dilute ($\varphi \leq 0.03$) suspensions of the larger hydrogenated (*h*-PBM1) and, separately, the smaller deuterated spheres (*d*-PBM14) at various scattering length densities ρ_m between $\rho_m = -0.03 \times 10^{-4}$ nm^{-2} and 1.24×10^{-4} nm^{-2}. The suspension medium was a mixture of *cis* h_{18}-decalin and d_{18}-octane. Under these conditions the large hydrogenated spheres are only weakly scattering with the matchpoint, where the extrapolated $q = 0$ intensity vanishes, at approximately $\rho_m \sim 1.04 \pm 0.02 \times 10^{-4}$ nm^{-2}. Conversely, the small deuterated spheres are far from match and are strong scatterers at all the medium contrasts used here.

The experimental form factors were modeled in terms of an internal core–shell structure. Polydispersity was treated as described in Sec. III A. The polydispersity σ_c of the core radius distribution was chosen so that the variation in the overall (core plus shell) radius was as found by transmission electron microscopy. This gave an effective core radius polydispersity σ_c, for component A and B, as 0.04 and 0.16, respectively. The core was taken as either hydrogenated or deuterated PMMA with an associated scattering length density ρ_c given in Table III. The thickness of the shell Δ was fixed for both sets of particles at the value found above of $\Delta = 8.9$ nm. The remaining parameters were determined from a least squares fit of the experimental form factors to the polydisperse core–shell model [Eq. (18)]. Corrections for instrumental smearing and multiple scattering were included by the methods described in Sec. II B.

The mean core radius $\bar{r}_c$ was determined from measurements in *cis* h_{18}-decalin. In this solvent the shell is virtually matched and so gives practically no contribution to the scattered intensity. Fits to the experimental form factors gave the mean core radii, for component A and B, as 146.6 ± 0.3 and 37.5 ± 0.2 nm, respectively. With the core radius determined, the scattering length density of the shell ρ_s was found by matching the calculated and measured scattering curves. All comparisons were made in absolute units. The least squares fitted values of ρ_s for components A and B are plotted as a function of the medium contrast in Fig. 2. All other parameters were fixed at the values described above. The observation that the fitted values of ρ_s are not constant but vary, almost linearly, with the medium contrast ρ_m strongly supports the hypothesis that the shell contains solvated stabilizing chains. Since the scattering length densities of both PHS and *cis* h_{18}-decalin are close to zero, the values of ρ_s directly measure the average volume fraction of d_{18}-octane within the shell. For the data given in Fig. 2 this d_{18}-octane fraction varies between 0.05 and 0.25.

Figures 3 and 4 show a comparison between the calculated and experimental scattering curves for *h*-PBM1 and *d*-PBM14 at five different medium contrasts. The agreement is generally very good with all experimental form factors adequately modelled by a simple core–shell structure. However, the relatively poor fit to the form factor of the large spheres at $\rho_m = 1.24 \times 10^{-4}$ nm^{-2}, just above the intensity match point, suggests that a more sophisticated model for the graft-

TABLE III. Coherent scattering length densities (ρ).

Material	$\rho(10^{-4}/\text{nm}^{-2})$
h-PMMA	1.07
d-PMMA	7.02
h-PHS	−0.06
cis h_{18}-decalin	−0.03
d_{18}-octane	6.42

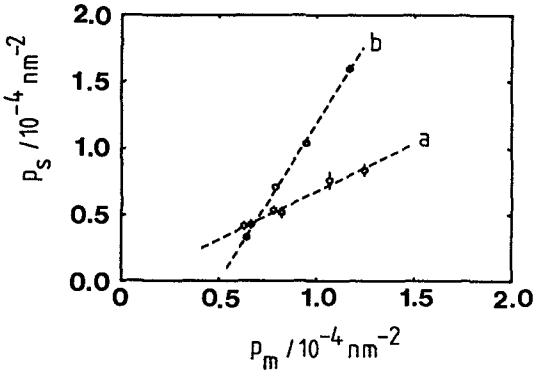

FIG. 2. Results from fitting the measured form factors of (a) *h*-PBM1 and (b) *d*-PBM14 spheres to the polydisperse core–shell model. The best-fit values for the scattering length density of the shell (ρ_s) are given as a function of the medium scattering length density (ρ_m). The dashed lines are drawn as guides to the eye.

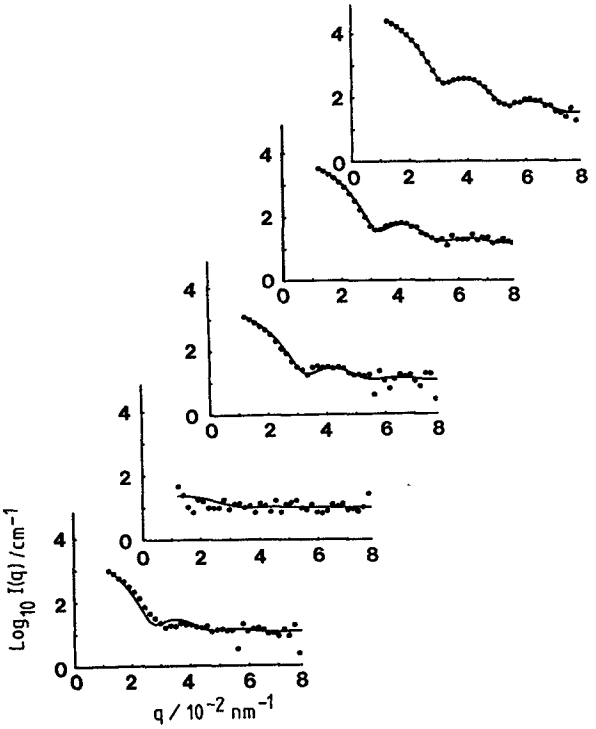

FIG. 3. The scattering intensities (points) measured from dilute ($\varphi = 0.03$) suspensions of the large hydrogenated spheres (h-PBM1) at medium scattering length densities of, from top to bottom, -0.03, 0.63, 0.78, 1.02, and 1.24×10^{-4} nm^{-2}. The solid lines are the results of a least-squares fit to the polydisperse core–shell model described in the text.

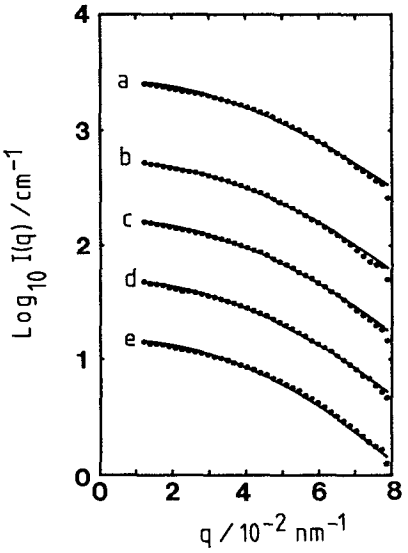

FIG. 4. Comparison of the experimental form factor (points) of the small deuterated spheres (d-PBM14) with the results (solid lines) calculated from the polydisperse core–shell model. The scattering length density of the suspension medium was (in units of 10^{-4} nm^{-2}) (a) -0.03, (b) 0.64, (c) 0.79, (d) 0.95, and (e) 1.17. The curves have been scaled so that the intensity levels are for the same colloid number density as the data of Fig. 3. For the sake of clarity each curves has been shifted by (a) $+0.5$, (b) 0.0, (c) -0.5, (d) -1.0, and (e) -1.5 units vertically.

ed layer structure may be necessary to accurate reproduce data both above and below match. Nevertheless, for the contrasts considered here the simple core–shell model is seen to be adequate.

B. SANS measurements

The structure of the colloidal crystals formed by a binary mixture of spheres of diameter ratio $\alpha\sim0.31$ (suspension 1 in Table II) was studied by contrast variation techniques. Large protonated spheres were mixed with smaller deuterated spheres (B) in the proportions AB_4 in a suspension of total volume fraction 0.61. Within a few hours the binary mixture showed a significant degree of crystallization, and after a day the sample volume was completely filled with small crystallites. SANS measurements were made on five such samples, with nominally identical component volume fractions and medium scattering length densities of -0.03, 0.63, 0.79, 1.02, and 1.24×10^{-4} nm^{-2}.

The scattered intensity from each of the five different contrast measurements may be concisely written in a matrix notation as

$$\mathbf{I}(q) = \mathbf{P}(q)\cdot\mathbf{S}(q) \tag{29}$$

following Eq. (26). Here $\mathbf{I}(q)$ is a five-dimensional column vector consisting of the individual scattering intensities $d\Sigma/d\omega(q)$, $\mathbf{P}(q)$ is a 5×3 matrix of form factors with the

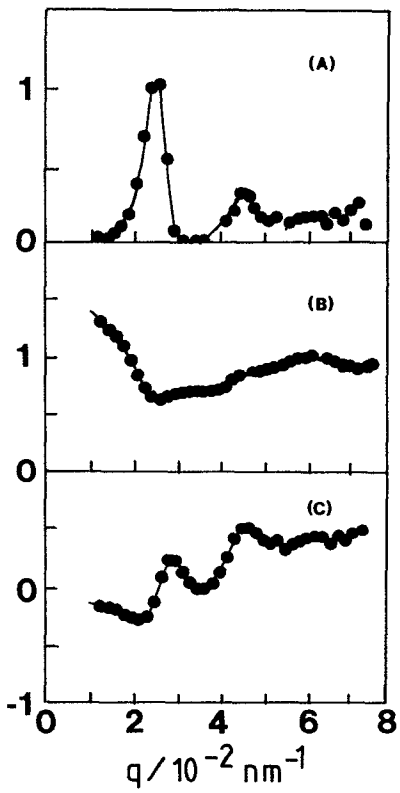

FIG. 5. The experimentally determined partial structure factors (a) $\bar{S}_{AA}$, (b) $\bar{S}_{BB}$, and (c) $\bar{S}_{AB}$ of the (partially) crystalline mixture of composition AB_4 and total volume fraction 0.61. Here A refers to the large hydrogenated spheres (h-PBM1) and B labels the smaller deuterated component (d-PBM14). The solid lines are guides to the eye.

rows $\{n_A \overline{F_A^2}(q),\ 2[n_A n_B \overline{F_A^2}(q)\,\overline{F_B^2}(q)]^{1/2},\ n_B \overline{F_B^2}(q)\}$, and the vector of structure factors is given by $\mathbf{S}^T(q) = [\bar{S}_{AA}(q), \bar{S}_{AB}(q), \bar{S}_{BB}(q)]$. Inversion of this matrix equation, at each value of q, gives the corresponding partial structure factors. Here the solution is overdetermined with five equations for the measured intensities expressed in terms of just three unknown structure factors.

Attempts to solve these matrix equations by standard least-squares techniques were, however, unsatisfactory. There was a significant amplification of experimental errors, particularly in the derived $\bar{S}_{AA}$, and to a lesser extent, the $\bar{S}_{AB}$ structure factors. As one might physically expect, the least squares estimates of $\bar{S}_{AA}$ and $\bar{S}_{AB}$ were most sensitive to errors near the minima in the large sphere form factors ($q \sim 0.03$ and $0.05\ \mathrm{nm}^{-1}$) and at high q. This sensitivity, in severe cases, resulted in unphysical values for the large sphere self structure factor. To avoid these difficulties, partial structure factors were chosen[34] which minimized the weighted sum of the squares of the discrepancy between calculated and measured intensities *and* satisfied the conditions of Eq. (28). This ensured that the calculated intensities were always positive at all medium contrasts. The corresponding *constrained* structure factors differed from the least-squares estimates only in the particular case of $\bar{S}_{AB}(q)$ for $q \geqslant 0.045\ \mathrm{nm}^{-1}$ and $\bar{S}_{AA}(q)$ for $q \geqslant 0.03\ \mathrm{nm}^{-1}$. There was no noticeable change in $\bar{S}_{BB}(q)$. The resulting partial structure factors are plotted in Fig. 5. The internal consistency of the measured data is illustrated in Fig. 6 by the close agreement between the intensities calculated from the fitted structure factors (solid lines) and those measured (points). The fact that the data may be adequately represented in terms of just three functions supports our assertion (Sec. III C) that the contrast dependence of the polydisperse structure factors may be ignored.

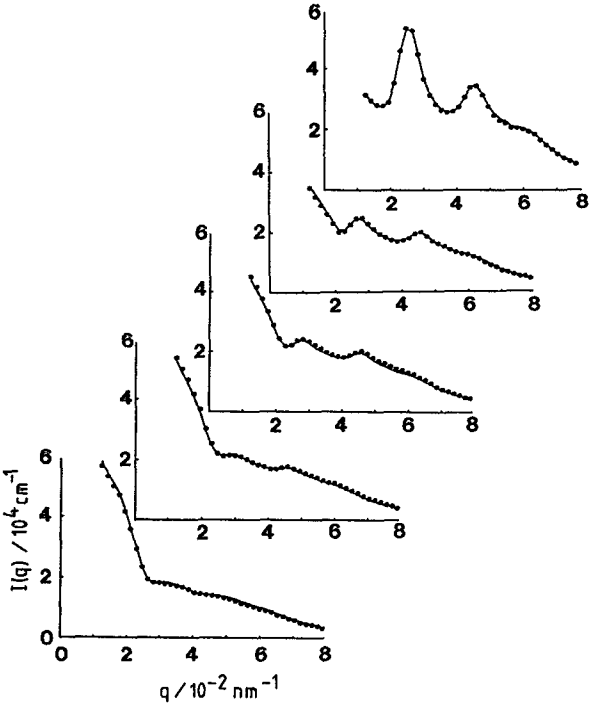

FIG. 6. Comparison of the experimental scattered intensities (points) with the results calculated (solid lines) from the partial structure factors given in Fig. 5. The curves correspond to the scattering from a bimodal mixture of composition AB_4 and volume fraction 0.61 at medium contrasts of, from top to bottom, -0.03, 0.63, 0.79, 1.02, and $1.24 \times 10^{-4}\ \mathrm{nm}^{-2}$.

To understand these findings, consider first the form of $\bar{S}_{AA}$, the self-structure factor of the large spheres. $\bar{S}_{AA}$ presents a classical shape with a low value approaching $q = 0$ and peaks at $q \sim 2.5 \times 10^{-2}$ and $4.6 \times 10^{-2}\ \mathrm{nm}^{-1}$, which reflect the strong spatial correlations between the large spheres in the crystalline structure. The origin of these peaks is clearly seen from light scattering measurements on the same samples. Light scattering experiments (which were sensitive only to the positions of the large spheres, i.e., $\bar{S}_{AA}$) showed sharp Bragg reflections typical of single component hard sphere colloidal crystals.[7] The most intense peak was the interplane (001) reflection, indexed on a hexagonal basis, which occured at a wave vector of $\sim 2.29 \times 10^{-2}\ \mathrm{nm}^{-1}$. Reflections were also expected at approximately $3.74 \times 10^{-2}\ \mathrm{nm}^{-1}$ (110), $4.39 \times 10^{-2}\ \mathrm{nm}^{-1}$ (111), and $4.58 \times 10^{-2}\ \mathrm{nm}^{-1}$ (002). These Bragg reflections are broadened into the peaks observed by SANS at $q \sim 2.5$ and $4.6 \times 10^{-2}\ \mathrm{nm}^{-1}$ because of the much lower resolution of neutron as compared to light scattering measurements (cf. Secs. II B and II C). Finally, we note that the measured asymptotic value of $\bar{S}_{AA}$ was nearly 0.3, which differs from the theoretical value 1. This disagreement is probably due to a systematic experimental error. As is often done in the literature, we could have corrected our values of $\bar{S}_{AA}$ by a multiplicative constant.

In comparison the small sphere structure factor $\bar{S}_{BB}$ is very different. First, it displays no strong interference peaks and secondly rather than a low value at $q = 0$ $\bar{S}_{BB}$ shows a rise which suggests a long range clustering among the smaller spheres. The absence of Bragg reflections demonstrates that the small spheres were not present in any appreciable numbers in the crystallites which were apparent to the eye. With, for example, a NaCl structure present strong correlation peaks would be expected in $\bar{S}_{BB}$ at the same scattering vectors as found in $\bar{S}_{AA}$, i.e., 2.3×10^{-2}, 3.7×10^{-2}, and $4.4 \times 10^{-2}\ \mathrm{nm}^{-1}$, etc. The form of $\bar{S}_{BB}$ and the cross structure factor $\bar{S}_{AB}$ can, however, be understood in terms of the structures expected for a fluid assembly of very differently sized large and small spheres.

Within the Percus–Yevick (PY) approximation, Biben and Hansen[35] have shown that when $\sigma_B/\sigma_A \to 0$, the small sphere structure factor $S_{BB}(q)$ approaches the limiting form

$$S_{BB}(q) = S^*_{BB}(q) + \frac{6}{\pi\sigma_B^3}\frac{\varphi_A\varphi_B}{1-\varphi_A}\delta(\mathbf{q}). \tag{30}$$

Here $S^*_{BB}(q)$ is the PY structure factor for a homogeneous one-component fluid of small spheres with an effective volume fraction $\varphi^*_B = \varphi_B/(1-\varphi_A)$, which is just the small sphere volume fraction once the volume occupied by the larger spheres has been subtracted. The delta function $\delta(\mathbf{q})$ describes the confinement of the small spheres within the interstities of the neighboring shell of large spheres. This expression, although valid in the limit $\sigma_B/\sigma_A \to 0$, describes

the salient features of the observed small sphere structure factor rather well. For an inhomogeneity on the scale of the large sphere (i.e., 311 nm) we expect a sharp peak at the origin, of width $2\pi/311 \sim 0.02\ \text{nm}^{-1}$, as observed. In addition away from $q \sim 0$, S_{BB} should approach the effective one-component structure factor S^*_{BB}, which has a maximum at a scattering vector of $2\pi/\sigma_B \sim 0.065\ \text{nm}^{-1}$, as is evident in the experimental data.

A full comparison between theory and experiment requires calculations for mixtures with both finite diameter ratios and size polydispersity. For the hard sphere interaction analytic expressions have been derived by Vrij[36] for the scattering functions in an arbitrary multicomponent mixture within the PY approximation. These results are readily generalized to treat a bimodal mixture of hard spheres representative of *h*-PBM1 ($\bar{d}_A = 311$ nm, $\sigma_A = 0.04$) and *d*-PBM14 ($\bar{d}_B = 93$ nm, $\sigma_B = 0.13$). The inherent size polydispersity of each component has been modeled by taking a Schulz distribution of hard sphere diameters with the same mean and polydispersity as the experimental system. It was assumed that each particle had an internal core–shell structure with the scattering parameters determined in Sec. IV A. The resulting polydisperse PY structure factors for a suspension of partial volume fraction $\varphi_A = 0.45$ and $\varphi_B = 0.053$ (composition AB_4) is plotted in Fig. 7. In order to ensure the calculated structure factors are directly comparable with the measured data in Fig. 5, the theoretical results have been smeared by the procedures described in Sec. II B.

The qualitative agreement between the small sphere structure factors ($\bar{S}_{BB}$ and $\bar{S}_{AB}$) in Figs. 5 and 7 is particularly striking. Evidently, in the experimental sample the small spheres are present in a fluid rather than a crystalline environment.

C. Light scattering measurements

Independent evidence for the size separation of big and small spheres was obtained from light scattering under conditions in which the scattering from the large spheres predominated. This is readily achieved since, away from match, the small sphere scattering is lower by a factor of approximately α^6 (i.e., $\sim 2 \times 10^{-3}$) as compared with a large sphere of the same profile. Hence light scattering experiments are sensitive, in the main, only to the large sphere correlations (i.e., $\bar{S}_{AA}$). Such measurements are complementary to the neutron scattering results where experimental conditions were deliberately chosen so as to reveal the structures formed by the smaller component.

Light scattering measurements were made on four colloidal samples (labeled 2–5 in Table II) with a large sphere volume fraction (nominally) fixed at $\varphi_A = 0.539$ and differing amounts of a second smaller component B. Overall suspension compositions were A, $AB_{1.4}$, $AB_{2.0}$, and $AB_{2.8}$. The hard sphere diameter ratio was estimated as $\alpha \sim 0.36$. When left undisturbed, all four samples crystallized. Crystallization was nucleated homogeneously throughout the samples and small crystallites of size 10–30 μm formed and completely filled the available volume.

The measured scattering intensities are plotted in Fig. 8,

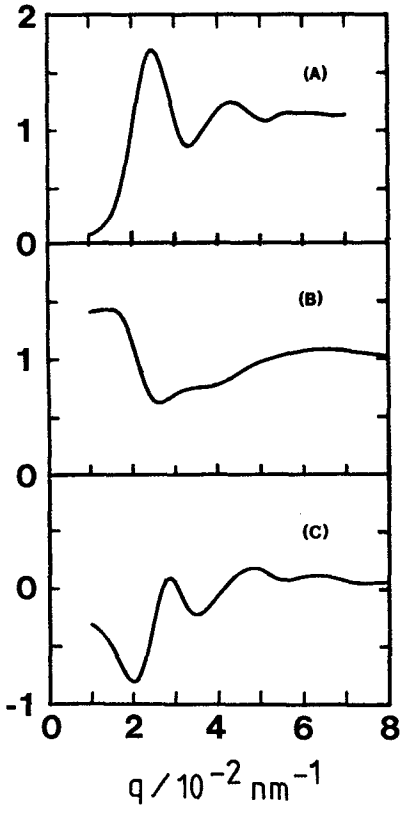

FIG. 7. Polydisperse structure factors (a) $\bar{S}_{AA}$, (b) $\bar{S}_{BB}$, and (c) $\bar{S}_{AB}$ calculated from the Percus–Yevick approximation for a fluid mixture of hard spheres of composition AB_4 and total volume fraction 0.51. The larger spheres (A) have a mean diameter of 311 nm and a size polydispersity of 0.04 while the smaller spheres (B) are 93 nm in diameter with a polydispersity of 0.13.

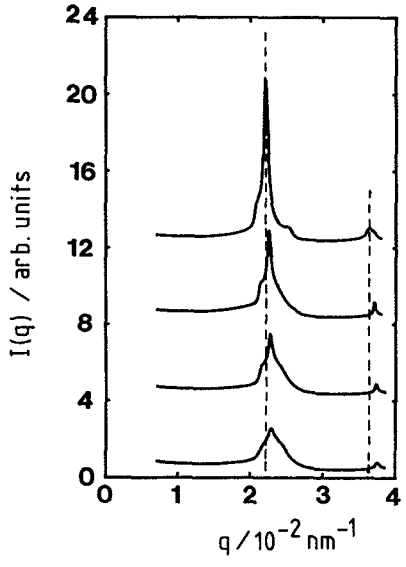

FIG. 8. The measured light scattering intensity from mixtures of composition A, $AB_{1.4}$, $AB_{2.0}$, and $AB_{2.8}$ (top to bottom) as a function of the scattering vector q. The partial volume fraction of the large spheres (A) was the same in all mixtures, $\varphi_A = 0.54$. The dashed lines denote the positions of the first two sharp Bragg reflections in the pure single component crystal of large spheres.

displaced for ease of comparison. All four diffraction patterns are similar in form. Two sharp Bragg reflections, at $q_{(001)} \sim 2.3 \times 10^{-2}\,\mathrm{nm}^{-1}$ and $q_{(110)} \sim 3.7 \times 10^{-2}\,\mathrm{nm}^{-1}$, are evident together with a broad background of diffuse scattering. Similar diffraction patterns have been observed in single component colloidal crystals and have been interpreted in terms[7] of a random stacked crystal of close packed planes of spheres. As is evident from Fig. 8 the crystalline order of the large spheres is relatively unaffected by the addition of the second smaller component. The large spheres even in the presence of the small spheres remain at the vertices of a random stacked crystal which is structural very similar to that formed in the absence of small spheres. Indexing the reflections in Fig. 8 on this basis gives the length of the equivalent face centred cubic unit cell (equal to $\sqrt{2}$ times the large sphere separation) as 490, 480, 477, and 475 nm in the crystals formed by the suspensions of composition A, $AB_{1.4}$, $AB_{2.0}$, and $AB_{2.8}$. It is apparent that the large sphere interparticle spacing in the the solid phase contracts as the smaller component is added. The effect is, however, pretty small with the unit cell shrinking by at most 3.2%. As one might physically guess, this suggests that the smaller spheres are not present to any significant degree in the crystal of large spheres. To see this we consider results from two simple analytical models for hard sphere freezing.

Ermak *et al.*[37] have demonstrated that if the smaller component is soluble in the large sphere crystal the unit cell of the coexisting solid lattice expands as small particles are introduced. The expansion is greater the bigger in size the small component is. However, the effect is fairly small. For example, when the small component is present at about a mole fraction of 0.5 in both coexisting phases, the unit cell expansion is a little bit less than 1% for point particles and slightly more than 1% for spheres of diameter ratio $\alpha = 0.1$. In this model the fluid phase is enriched in small spheres while the coexisting solid is correspondingly depleted. Similar conclusions have been reached by Xu and Baus[38] from a density functional treatment of hard sphere freezing within the PY approximation. For diameter ratio in the range $0.2 < \alpha < 0.5$ where both the PY approximation is expected to hold and their model is still meaningful the presence of a finite concentration of small spheres lowers the density of the large sphere lattice.

If conversely spheres of the smaller component are insoluble in the large sphere crystal then the unit cell of the coexisting solid lattice is expected to contract. This increase in the density of the large sphere lattice has been both predicted[39] and confirmed experimentally.[18] A detailed discussion of the immiscible sphere model has been described previously[39] for $\alpha = 0.65$ and 0.85. Here, however, the fluid–solid phase equilibria is presented for mixtures of very different sized spheres. Utilizing simulation results for hard spheres in the fluid and solid phases[40] and equating the pressure and chemical potential of the larger component in both phases leads to the phase diagrams plotted in Fig. 9. The addition of small particles is seen to increase the density of

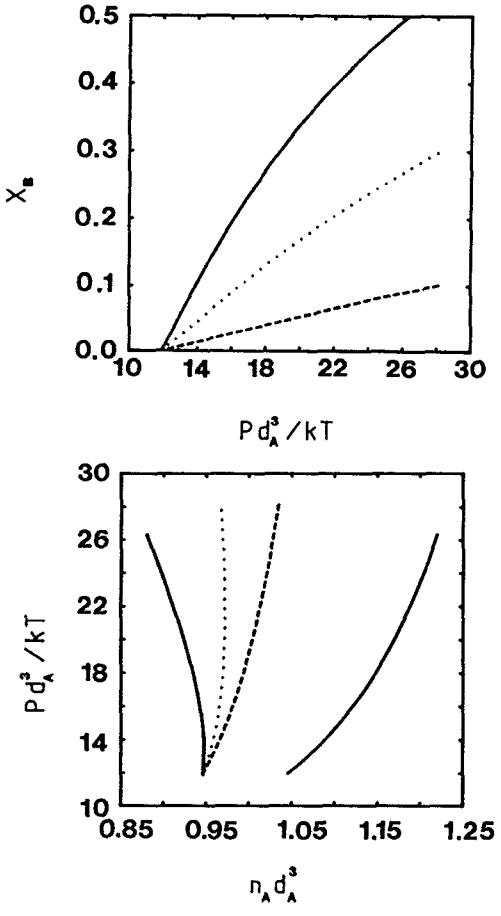

FIG. 9. Phase diagrams calculated from the immiscible hard sphere model, described in the text, for binary mixtures of diameter ratio 0.4 (solid lines), 0.3 (dotted lines), and 0.2 (dashed lines). In the upper part the mole fraction of small spheres x_B in the initial suspension is given as a function of the osmotic pressure, in units of kT/d_A^3, where d_A is the diameter of the larger spheres. The lower figure gives the density of the larger spheres in the coexisting fluid and crystal of large spheres (in units of d_A^{-3}) in terms of the osmotic pressure.

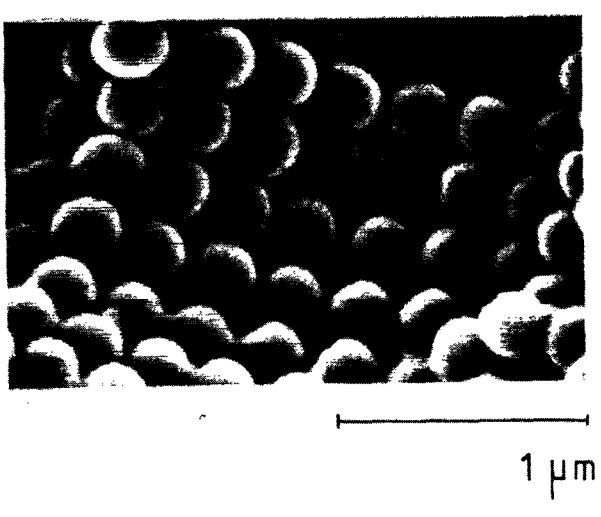

FIG. 10. Scanning electron micrograph of the colloidal crystal formed in a mixture of composition $AB_{2.0}$. Note that most of the interstitial sites in the crystal of large spheres are vacant.

the coexisting solid phase. This increase in density is most striking for mixtures of hard spheres with small diameter ratios and a high proportion of small spheres. For a diameter ratio of $\alpha \sim 0.36$, when each component is present in equal numbers in the fluid phase (i.e., $x_B = 0.5$) the unit cell of the large sphere lattice contracts by approximately 4%.

On the basis of these calculations it seems reasonable to assume that the spheres of the smaller component are not soluble to any significant degree in the large sphere crystals. This observation correlates well with the SANS measurements described in Sec. IV B. The immiscible hard sphere model predicts both the direction of the large sphere lattice parameter change as well as furnishing a reasonable estimate of its magnitude. This simple model is, however, only in qualitative, rather than quantitative, agreement with the data. Detailed calculations predict lattice parameter reductions of 5.3%, 7.0%, and 7.6% for the three binary suspensions. The corresponding experimental values are 2.1%, 2.8%, and 3.2%. It is possible that this behavior is either a result of inaccuracies in the present model or may suggest there is a small, but significant, degree of mutual solubility. Scanning electron micrographs of dried-down colloidal samples, reproduced in Fig. 10, suggest only a very limited degree of small sphere solubility in the crystal of large spheres.

V. CONCLUSIONS

The present experiments demonstrate that a binary suspension of colloidal spheres of diameter ratio $\alpha = 0.31$ do not form interstitial crystals although such structures are geometrically feasible. Instead on freezing, there is a size separation with the large spheres forming a crystalline structure while the smaller spheres are excluded from the crystal into a second (coexisting) fluid phase. Partial structure factors have been determined from small-angle neutron scattering measurements. These may be qualitatively described by a hard sphere model for the interaction potential between all colloidal components. A simple analytical model for the phase equilibria predicts that the interparticle spacing in the large sphere crystal should contract as further small spheres are added. This has been confirmed by light scattering measurements. Scanning electron microscopy on dried colloidal crystals show that the small spheres are predominantly insoluble in a crystal of large spheres.

ACKNOWLEDGMENTS

We are particular grateful to Professor P. N. Pusey and Dr. A. R. Rennie for their generous help with the light and small-angle neutron scattering measurements. Finally, we thank the SERC and MOD for support of this work and to the Institute Laue-Langevin for the use of neutron facilities.

[1] S. Hachisu, Y. Kobayashi, and A. Kose, J. Colloid Interface Sci. **42**, 342 (1973).
[2] W. Luck, M. Klier, and H. Wesslau, Ber. Bunsenges. Phys. Chem. **67**, 75 (1963); I. M. Krieger and F. M. O'Neill, J. Am. Chem. Soc. **90**, 3114 (1968).
[3] For a review, see P. N. Pusey, in *Liquids, Freezing and the Glass Transition*, Les Houches, Session LI, 1989, edited by J. P. Hansen, D. Levesque, and J. Zinn-Justin (Elsevier, Amsterdam, 1991), p. 763–942.
[4] R. J. R. Cairns, R. H. Ottewill, D. W. J. Osmond, and I. Wagstaff, J. Colloid Interface Sci. **54**, 45 (1976); L. Antl, J. W. Goodwin, R. D. Hill, R. H. Ottewill, S. M. Owens, and S. Papworth, Colloid Surf. **17**, 67 (1986).
[5] P. N. Pusey and W. van Megen, Nature (London) **320**, 340 (1986).
[6] S. E. Paulin and B. J. Ackerson, Phys. Rev. Lett. **64**, 2663 (1990).
[7] P. N. Pusey, W. van Megen, P. Bartlett, B. J. Ackerson, J. G. Rarity, and S. M. Underwood, Phys. Rev. Lett. **63**, 2753 (1989).
[8] I. Livsey and R. H. Ottewill, Colloid Polym. Sci. **267**, 421 (1989).
[9] W. G. Hoover and F. H. Ree, J. Chem. Phys. **49**, 3609 (1968).
[10] For a recent review of the density functional method see, D. W. Oxtoby, in *Liquids, Freezing and the Glass Transition*, Les Houches, Session LI, 1989, edited by J. P. Hansen, D. Levesque, and J. Zinn-Justin (Elsevier, Amsterdam, 1991), p. 145–191.
[11] J. F. Lutsko and M. Baus, Phys. Rev. Lett. **64**, 761 (1990).
[12] X. C. Zeng and D. W. Oxtoby, J. Chem. Phys. **93**, 4357 (1990).
[13] A. R. Denton and N. W. Ashcroft, Phys. Rev. A **42**, 7312 (1990).
[14] W. G. T. Kranendonk, and D. Frenkel, Mol. Phys. **72**, 679 (1991).
[15] S. J. Smithline and A. D. J. Haymet, J. Chem. Phys. **86**, 6486 (1987); **88**, 4104 (E) (1988).
[16] S. W. Rick and A. D. J. Haymet, J. Chem. Phys. **90**, 1188 (1989).
[17] B. Brami, F. Joly, J. L. Barrat, and J. P. Hansen, Phys. Lett. A **132**, 187 (1988).
[18] P. Bartlett, R. H. Ottewill, and P. N. Pusey, J. Chem. Phys. **93**, 1299 (1990).
[19] P. N. Pusey and P. Bartlett (to be published, 1991).
[20] D. J. Cebula, J. W. Goodwin, R. H. Ottewill, G. Jenkin, and J. Tabony, Colloid. Polym. Sci. **261**, 555 (1983).
[21] E. Dickinson and R. Parker, J. Phys. Lett. (Paris) **46**, L229 (1985); J. L. Barrat and J. P. Hansen, ibid. **47**, 1547 (1986); R. McRae and A. D. J. Haymet, J. Chem. Phys. **88**, 1114 (1988).
[22] P. N. Pusey, J. Phys. (Paris) **48**, 709 (1987).
[23] K. Ibel, J. Appl. Crystallogr. **9**, 296 (1976).
[24] J. A. Miller, S. L. Cooper, C. C. Han, and G. Pruckmayr, Macromolecules **17**, 1063 (1984).
[25] V. Ramakrishnan, J. Appl. Crystallogr. **18**, 42 (1985).
[26] J. S. Pedersen, D. Posselt, and K. Mortensen, J. Appl. Crystallogr. **23**, 321 (1990).
[27] J. Schelten and W. Schmatz, J. Appl. Crystallogr. **13**, 385 (1980).
[28] J. B. Hayter, in *Physics of Amphiphiles: Micelles, Vesicles and Microemulsions*, edited by V. Degiorgio (North Holland, Amsterdam, 1985).
[29] See, for example, L. C. Roess and C. G. Shull, J. Appl. Phys. **18**, 308 (1947).
[30] B. H. Zimm, J. Chem. Phys. **16**, 1099 (1948).
[31] S. R. Aragon and R. Pecora, J. Chem. Phys. **64**, 2395 (1976).
[32] A. Guinier and G. Fournet, *Small-Angle Scattering of X-rays* (Wiley, New York, 1955).
[33] J. G. Kirkwood and F. P. Buff, J. Chem. Phys. **19**, 774 (1951).
[34] Routine EO4VDF, Numerical Algorithm Group, Oxford, England.
[35] T. Biben and J. P. Hansen, Europhys. Lett. **12**, 347 (1990).
[36] A. Vrij, J. Chem. Phys. **69**, 1742, (1978); **71**, 3267 (1979).
[37] D. L. Ermak, B. J. Alder, and L. R. Pratt, J. Phys. Chem. **85**, 3221 (1981).
[38] H. Xu and M. Baus, J. Phys. C **20**, L373 (1987).
[39] P. Bartlett, J. Phys. Condensed Matter **2**, 4979 (1990).
[40] G. A. Mansoori, N. F. Carnahan, K. E. Starling and T. W. Leland, J. Chem. Phys. **54**, 1523 (1971); D. A. Young and B. J. Alder, *ibid.* **70**, 473 (1979).